This is a peer-reviewed, accepted author manuscript of the following research article: Cheng, Y., Xi, C., Dai, S., Ji, C., Cocard, M., Yuan, Z., & Incecik, A. (2021). Performance characteristics and parametric analysis of a novel multi-purpose platform combining a moonpool-type floating breakwater and an array of wave energy converters. Applied Energy, 292, [116888]. https://doi.org/10.1016/j.apenergy.2021.116888

Performance characteristics and parametric analysis of a novel multi-purpose platform combining a moonpool-type floating breakwater and an array of wave energy converters

Yong Cheng[a], Chen Xi[a], Saishuai Dai[b,*] , Chunyan Ji[a], Margot Cocard[b], Zhiming Yuan[a, b], Atilla Incecik[b]

[a]*School of naval architecture and ocean engineering, Jiangsu University of Science and Technology, Zhenjiang, 212003, China*

[b]*Naval Architecture, Ocean and Marine Engineering Department, University of Strathclyde, Glasgow, United Kingdom*

ABSTRACT

Integration of Wave Energy Converters (WECs) with floating breakwater system provides a multi-function solution to wave energy extraction and offshore infrastructural protection. The contribution of this work is to guide the optimal size and configuration of a multi-purpose platform including a moonpool-type floating breakwater and an array of heaving oscillating-buoy (OB) WECs. The investigation is performed using a developed time-domain numerical wave tank (NWT) based on the three-dimensional (3D) potential flow theory with fully nonlinear boundary conditions on transient wetted body surfaces and free surfaces. The comparison of the hydrodynamic performance among the multi-purpose platform, the isolated array WECs, and the isolated floating breakwater are examined. The internal fluid motion in the moonpools has a positive effect on the wave energy absorption of WECs, which in turn enhances the wave attenuation capacity of the floating breakwater. WECs with larger diameter have a larger water-plane area, which leads to more extracted wave energy. The wave nonlinearity reduces the optimal PTO damping value and has an adverse effect on the wave energy extraction. However, when wave nonlinearity becomes prominent, the wave attenuation capacity is improved with increasing PTO damping. For an unequal layout of moonpools, the thinner moonpools are the major contributor to wave energy extraction, especially in the short wave region. As a result of mass exchange of fluid from the moonpool to the outer domain, the multi-purpose platform indicates favorable performance of wave energy absorption. The novel floating system makes the utilization of wave energy over a wider frequency range.

Keywords: Multi-purpose platform; Wave energy converter; Floating breakwater; Internal fluid motion; fully nonlinear simulation; Energy capture efficiency

1. Introduction

The world tragedy Coronavirus disease-2019 (COVID-19) has focused attention on vulnerable island communities whose conventional power source relies on imported fossil fuel and was deeply affected due to restricting transportation measures taken to fight the COVID-19. A dramatic drop in the GDP of those islands whose economic activities heavily rely on tourism urges us to identify a secondary income source for them to survive the economic crisis. At the same time, the International Energy Agency (IEA) conservatively predicts that the global CO2 emission will

*Corresponding author: Saishuai Dai, mainly research in hydrodynamic performance of marine energy devices
E-mail: saishuai.dai@strath.ac.uk

decrease by 8% through 2020 [1], as a result of the increasing share of renewable energy during the pandemic. This again emphasizes that renewable energy is the key to sustainable development. Wave energy is one of the four main marine renewable energy resources (wave energy, tidal energy, ocean thermal energy, and offshore wind energy) due to its high energy density, predictability, and wide-spread availability [2]. Although wave energy extracted technologies have been investigated and improved for more than three decades [3], the constructed cost of wave energy converters (WECs) is still very high compared to the cost of the conventional coal-burning power plant. Integrating WECs into existing maritime structures can achieve the reduction of construction cost, multi-function, and space-sharing. On the other hand, floating breakwaters as effective wave absorber devices can provide sea areas with small wave amplitude where extensive aquaculture farms can be installed due to the availability of space. Therefore, the multi-purpose platform combining floating breakwater and an array of WECs is a promising 'vaccine' to activate islands' immunity to expensive imported fossil fuel, providing clean and cheap power as well as seafood export as a secondary income source.

Floating breakwaters attenuate the incident waves through dissipating or reflecting the wave energy, whereas WECs extract the incident wave energy by transforming the wave energy into electricity generation. The proposed multi-purpose platform (MPP) regards the floating breakwaters as wave-energy-converting devices that aim to achieve the synergetic effects of wave energy extraction and wave attenuation. The MPPs can be classified into floating breakwater-oscillating water column (OWC) type WEC integrated platform, floating breakwater-oscillating buoy (OB) type WEC integrated platform, and floating breakwater-overtopping type WEC integrated platform. Neelamani et al. [4] experimentally investigated the pneumatic efficiency of a floating OWC caisson structure with an air chamber for reducing transmitted wave height and enhancing wave energy extraction. Subsequently, He et al. [5] proposed a rectangular box type breakwater with double OWC chambers: one on the weather side and the other on the leeward side of the integrated platform. Their measured data revealed that the energy extraction in the rear chamber is smaller than the one in the front chamber due to the reduction of air-pressure fluctuation. Later, He et al. [6] further analyzed the hydrodynamic performance of a configuration with asymmetric chambers (a narrower chamber on the weather side and a wider chamber on the leeward side). Along with the same designed ways, Howe et al. [7] considered multiple OWCs integrated into a π-type floating breakwater, and investigated the performance characteristics subjected to irregular wave loads. They found that the multiple chambers can provide an efficient approach to extend the wave frequency range over which wave energy is extracted. Xu and Huang [8] measured both the capture efficiency and the transmitted wave elevation of an integrated platform of a pile floating breakwater and an array of OWC WECs. Zheng et al. [9] developed an analytical solution using the eigenfunction matching method to investigate the effects of the chamber thickness on the wave energy absorption of a floating breakwater-OWC integrated system. All the above studies indicated that through integrating the air chamber into the floating breakwater, the high wave energy extraction and the effect wave absorption ability can be simultaneously achieved due to the resonant motion of the inside free surface. This brought illumination to the investigation in this paper, and a moonpool structure with the particular configuration for wave absorption was explored as a floating breakwater.

Floating breakwater-oscillating buoy (OB) type WEC integrated platform is generally designed through two methods, i.e. 1) imposing a PTO system on the pontoon-type floating

breakwater; 2) adding an isolated OB into the front side of the floating breakwater. Ning et al. [10] proposed an integrated system of a vertical pile-restrained box-type floating breakwater with a PTO system installed above the breakwater, and experimentally studied the effects of incident wave parameters and PTO damping characteristics on the capture efficiency and the heaving motion. Then, Zhao et al. [11] theoretically simulated the behavior of such integrated system, and similar conclusions were obtained. Madhi and Yeung [12] optimized the geometrical shape of the floating breakwater and proposed a floating wedge-shaped box called 'The Berkeley Wedge (TBW)' to reduce the viscous effects during the working process. Furthermore, to enhance the wave attenuation ability of the integrated system in long waves, Ning et al. [13] developed a potential flow model to investigate analytically the hydrodynamic performance of the dual-pontoon floating breakwater, which works as the principle of OB WECs. Martinelli et al. [14] considered an OB WEC heaving in the weather side of a π-type floating breakwater and the corresponding experimental results indicated that the superposition of the incident waves and the reflected waves can enhance the wave energy extraction. Nguyen et al. [15] presented a hybrid finite element-boundary element method in the frequency domain to investigate the performance of an array of raft WECs attached at the fore-end of a very large floating structure for extracting the wave energy and reducing the hydroelastic response. Zhang et al. [16] established a 2D two-phase numerical tank based on Navier-Stokes equations and volume of fluid (VOF) free surface capturing approach to study the energy extraction and wave attenuation of a dual-floating integrated platform, which consists of an OB WEC and a floating breakwater behind WEC. Reabroy et al. [17] also investigated experimentally the hydrodynamic performance of such a system. Results showed that the narrow gap between the WEC and the floating breakwater has a positive effect on capturing the efficiency of symmetric WEC due to wave resonance. As a general extension, Zhang et al. [18] studied numerically the effect of parabolic openings at the weather side of a floating breakwater on the energy harvest of an array of heaving OB WEC.

Notwithstanding the above investigations provide enlightening contributions to the integrated design of floating breakwater and WECs, current commercialized applications for this integrated technology are restricted yet. The main reason is that the capture efficiency of WECs is relatively low and the corresponding enhancement has not been fully solved. Recently, many studies are performed to enhance the capture efficiency by optimizing the geometrical shape of WECs [12, 14, 16, and 17], but it is not easy to obtain an obvious leap of efficiency i.e. 10%. Another innovative solution is to increase the energy density of the surface waves by gathering the wave energy to a local area i.e. moonpools. Moonpools are vertical opening structures through the floating bodies and are usually used as riser/pipeline-installing equipment and wave energy extraction devices. Ning et al. [19] studied the increase of wave energy density in a moonpool with an enclosed air chamber, showing that the wave motion in the moonpool can be significantly strengthened due to the piston-mode and sloshing-mode motion of a fluid. Shi et al. [20] further used a 3D analytical model based on a smooth auxiliary function approach to investigate the resonant characteristics of a fluid in the moonpool. It was demonstrated that the wave amplitude in the moonpool is mainly determined by the ratio of the moonpool length and width. Ravinthrakumar et al. [21] carried out an experiment to study the effects of moonpool size on the hydrodynamic interaction between the floating body and the fluid in the moonpool. The experimental results were compared to linear numerical results, showing that the heave motion can be amplified by six times due to second-order wave resonant response in the moonpool. Bull [22] used the 3D boundary element

method based on potential flow theory to predict the hydrodynamic coupling effects of a moonpool within a floating body and found that the internal water motions, including piston-mode and sloshing-mode, have a positive effect on the wave energy extraction. Zheng et al. [23] introduced a novel OB WEC with a covered moonpool and investigated the effect of the top aperture on energy absorption. It is obtained that the completed opening of the roof aperture results in a narrower bandwidth and a higher maximum energy extraction than the one with closed status. Liu et al. [24] put forward integration of a heaving point-absorber WEC and a vertical cylindrical-shaped moonpool platform and investigated the wave energy conversion of the moonpool buoy experimentally and numerically. The results revealed that the density of wave energy in the moonpool increases not only at a certain wave frequency but also at a moderate bandwidth. Previous investigations mainly focused on the hydrodynamic behavior of a single OB WEC integrated into a moonpool structure, and have neglected the wave energy captured features of an array layout, which has a profound significance for practical application of the multi-function platform. Moreover, there have been few reports to date on the impact of multi-moonpool resonance on the wave energy absorption of WECs.

In this paper, an innovative multi-purpose platform (as shown in Fig. 1) combining the function of both floating breakwater and WECs is proposed and investigated. A dual cylindrical pontoon-type floating breakwater is used as a base structure, in which two moonpools are created by three connected walls between two cylinders. Compared to the traditional floating breakwater, the concept is inspired by the moonpools that can further reduce the transmitted wave amplitude through the internal wave motion. In addition, when the incident wave frequency is closed to the natural oscillating frequency of the fluid in the moonpools, the violent oscillating motion of the internal fluid is generated, and thus, the wave energy can be collected in the moonpools. Then, an array of heaving OB WECs is placed in the moonpools and is integrated with the floating breakwater by using a hydraulic PTO system installed above the WECs. The heave motion of the WECs is driven under the internal waves and is controlled by the mechanical coefficients i.e. PTO stiffness and PTO damping through energy captured mechanism. On the other hand, the kinetic energy of the WECs can affect the wave attenuation of the floating breakwater to a certain extent. Therefore, as a hypothesis, there could exist an optimal size and layout of WECs, in which the wave energy extraction and wave transmission of the multi-purpose platform reach a desirable level.

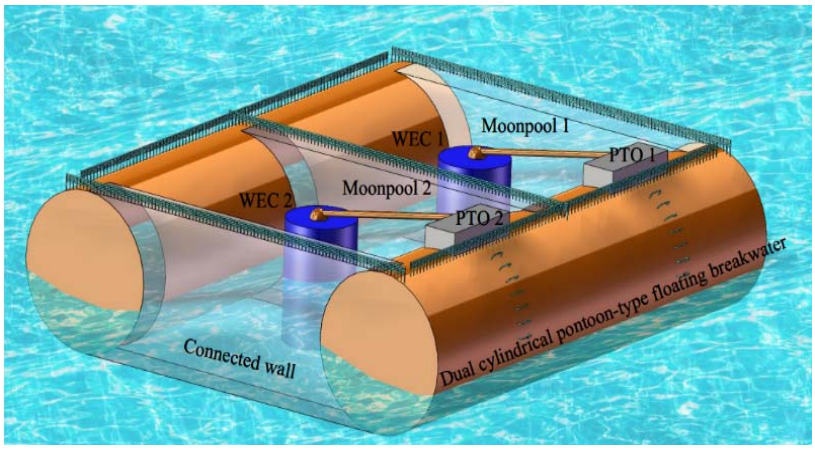

Fig. 1. Multi-purpose platform of a moonpool-type floating breakwater and an array heaving WECs

Prevised studies have primarily focused on the hydrodynamic performance of WECs

integrated on the weather side of single pontoon-type floating breakwaters. It is not possible to infer the effect of internal fluid motion in the moonpool-type floating breakwater on the energy extraction performance of the multi-purpose platform from existing studies. The novelty of this work is twofold: firstly to develop an accurate time-domain nonlinear model to optimize the design and configuration of moonpools generated by dual cylindrical pontoon-type platform, and secondly to obtain a more comprehensive understanding of the effects of internal fluid motion in moonpools on wave energy conversion of WECs and wave attenuation of floating breakwater through a series of parametric studies. This will help to achieve multi-purpose objective, which reduce significantly construction cost and make wave energy utilization more competitive.

The objective of this paper is to study the wave attenuation and the wave energy extraction of this multi-purpose platform. It should be mentioned that the hydrodynamics have specific characteristics compared with a single floating breakwater and isolated dual WEC system. An incident wave with moderate length can fully interact with the fluid in the moonpools, which leads to the resonant motion of the internal fluid and enhances the capture efficiency of WECs. Furthermore, the wave attenuation ability of the floating breakwater can be improved due to the energy transformation from the waves to the WECs. However, when the draft of the moonpool structure is small enough to the incident wavelength, the surface waves are usually entirely transmitted over moonpools, and the violent wave motion does not always occur inside of the moonpools. Therefore, this paper will analyze quantitatively the degree of the effect of the fluid motion in the moonpool on the capture efficiency, the WEC motion, and the transmitted coefficient. A time-domain higher-order boundary element method (HOBEM) is developed based on the potential flow theory with fully nonlinear body surface and water surface conditions. The hydrodynamics of the multi-purpose platform with different geometric parameters is optimized according to different wave parameters. This paper is structured as follows. In Section 2, the development of the numerical model is described detailedly. The convergent tests and the comparison with the published paper are given in Section 3. Then, Section 4 gives the calculated results and discussions for different designed parameters. Finally, the conclusions are summarized in Section 5.

2. Numerical method

2.1 Motion equations of WECs

As a preliminary hydrodynamic examination, a 3D regular wave obliquely interaction with a floating breakwater with two identical moonpools is considered in Fig. 2. A cylindrical OB WEC with only heaving motion is deployed on the center location of each moonpool using an independent PTO system, which forms an array of dual OB WEC system. Compared with WECs, the motion amplitude floating breakwater is small, and thus it is assumed to be fixed. In order to simulate accurately the transient motion of the WECs, three right-hand Cartesian coordinate systems including space-fixed $oxyz$ and each WEC-fixed $ox_iy_iz_i$ coordinates (i denotes the i-th WEC) are defined in Fig. 2. The motion equation of i-th WEC can be expressed as based on Newton's second law

$$M^i \ddot{\xi}^i = F_h^i + F_e^i \tag{1}$$

where M^i is the mass of i-th WEC, and $\ddot{\xi}^i$ is corresponding heaving acceleration. F_h^i and F_e^i

represent the hydrodynamic force and the external force, respectively.

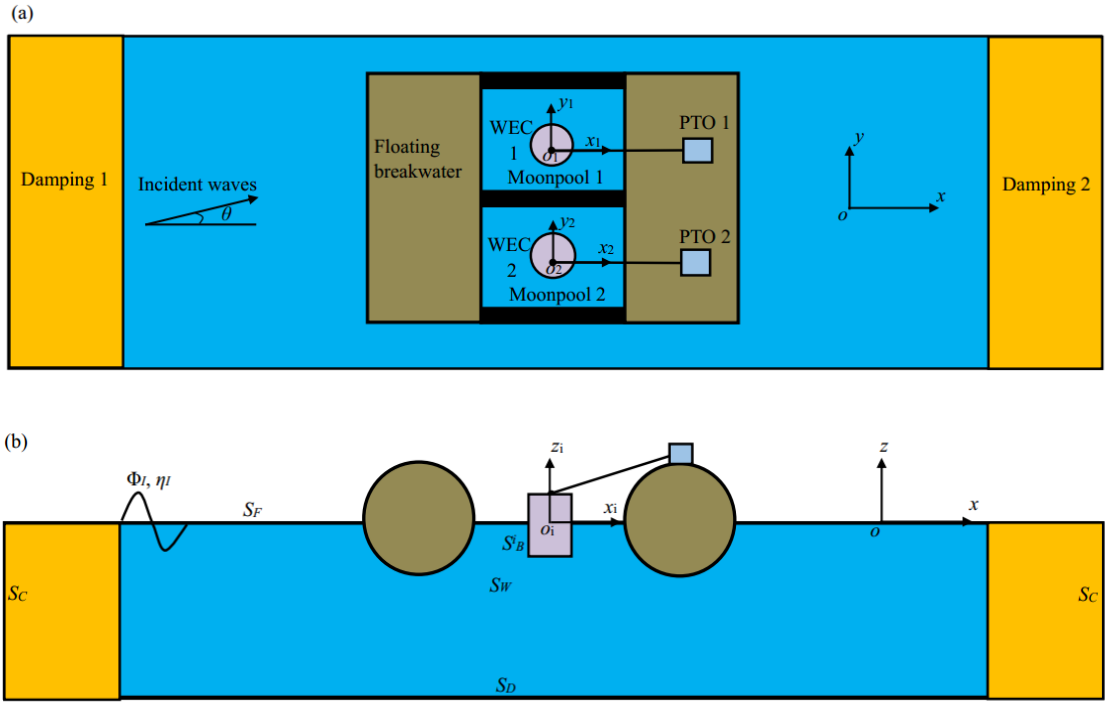

Fig. 2. A diagram of oblique waves interact with the multi-purpose platform in a 3-D wave tank: (a) Top view and (b) Side view

The heaving motion of WECs is converted into the flow of a liquid at high pressure by driving a hydraulic PTO system which includes a hydraulic cylinder, a high-pressure gas accumulator, a low-pressure gas accumulator and a hydraulic motor, as shown in Fig. 3. The highly fluctuating hydraulic energy produced by the reciprocating piston, can be smoothed by using the gas accumulator systems that provide a stable production and electrical power. The hydraulic motor controls the operation of an electric generator. A rectifying value system prevents liquid from leaving the high-pressure gas accumulator at *E* and from entering the low-pressure gas accumulator at *D*. In this study, the linear PTO system is considered and F_e^i is denoted as

$$F_e^i = -b_{pto}^i \dot{\xi}^i - c_{pto}^i \xi^i \tag{2}$$

where $\dot{\xi}^i$ and ξ^i represent the velocity and displacement of *i*-th WEC, respectively. b_{pto}^i and c_{pto}^i are the mechanical damping and stiffness coefficients of *i*-th WEC, respectively.

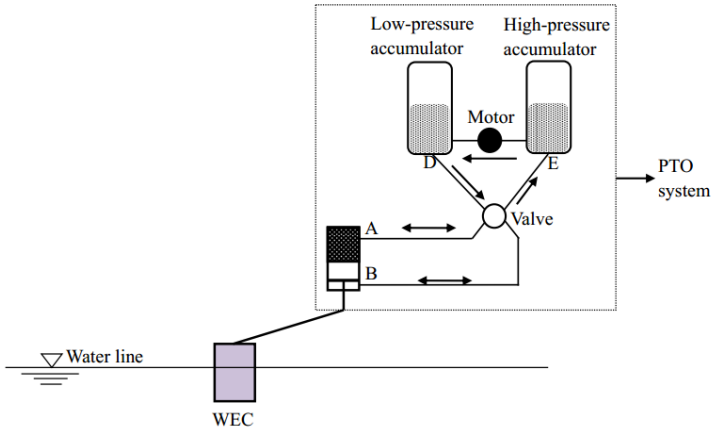

Fig. 3. Hydraulic PTO system

hydrodynamic force F_h^i denotes the force induced by the waves in the corresponding moonpool and can be obtained by integrating fluid pressure over the body wetted boundary

$$F_h^i = -\rho \iint_{S_B^i} \left(\frac{\partial \Phi^i}{\partial t} + \frac{1}{2}\left|\nabla \Phi^i\right|^2 + gz\right) \cdot n_z^i dS \tag{3}$$

Where ρ is the water density, g is the acceleration due to gravity force, n_z^i is defined as the unit normal vector along heaving direction, S_B^i is wetted surface of i-th WEC and Φ^i is the total velocity potential whose gradient is the velocity of water particle.

2.2 Integral equation of water motion

Based on the scattering principle of potential flow theory, the velocity potential is divided into two components i.e. incident waves Φ_I and scattering waves Φ_S. A 3D numerical water tank (NWT) which includes the water-free surface S_F, the wetted surface S_W of the floating breakwater, the wetted surface S^i_B of WECs, the tank lateral surfaces S_C, and the tank bottom surface S_D is established, and the incident potential Φ_I is known according to the analytical definition of the incident wave field. When fully nonlinear motion conditions are considered, the remaining scattering potential Φ_S satisfies the Laplace governing equation and the following boundary conditions:

$$\frac{d(x,y)}{dt} = \frac{\partial \Phi_S}{\partial (x,y)} + \frac{\partial \Phi_I}{\partial (x,y)} - \nu(r)\left[(x,y) - (x_0, y_0)\right] \quad \text{on } S_F \tag{4}$$

$$\frac{d\eta_S}{dt} = \frac{\partial \Phi_S}{\partial z} + \frac{\partial \Phi_I}{\partial z} - \frac{\partial \eta_I}{\partial z} - \nabla \Phi_I \cdot \nabla \eta_I - \nabla \Phi_S \cdot \nabla \eta_I - \nu(r)\eta_S \quad \text{on } S_F \tag{5}$$

$$\frac{d\Phi_S}{dt} = \frac{1}{2}\left|\nabla \Phi_S\right|^2 - \frac{1}{2}\left|\nabla \Phi_I\right|^2 - \frac{\partial \Phi_I}{\partial t} - (\eta_I + \eta_S) - \nu(r)\Phi_S \quad \text{on } S_F \tag{6}$$

$$\frac{\partial (\Phi_S + \Phi_I)^i}{\partial n} = \dot{\xi} \cdot n_z^i \quad \text{on } S^i_B \tag{7}$$

$$\frac{\partial (\Phi_S + \Phi_I)}{\partial n} = 0 \quad \text{on } S_W \text{ and } S_D \tag{8}$$

where η is the free surface elevation, the damping coefficient $v(r)$ is a modulation function which gradually absorbs scattering waves (Φ_S and η_S) at two ends of the tank, and (x_0, y_0, z_0) denotes the spatial location of the water particle at time t=0. d/dt is the material derivative defined by $d/dt=\partial/\partial t+\nabla\phi\cdot\nabla$. Because the whole simulation is conducted in the time-domain, the initial water surface conditions should be satisfied as follows:

$$\Phi\big|_{t=0}=\Phi_I, \qquad \eta\big|_{t=0}=\eta_I \tag{9}$$

Then, the integral equation of the water motion based on the above boundary value problem can be obtained using the second Green's law

$$\chi(\mathbf{p})\Phi_S(\mathbf{p})=\iint_S G(\mathbf{p},\mathbf{q})\frac{\partial\Phi_S(\mathbf{q})}{\partial n}-\phi(\mathbf{q})\frac{\partial G(\mathbf{p},\mathbf{q})}{\partial n}ds \tag{10}$$

where S denotes the whole boundary surface of the computational domain. $\mathbf{p}(x_s, y_s, z_s)$ and $\mathbf{q}(x_f, y_f, z_f)$ are the source and field points, respectively. χ is the solid angle coefficient which is decided according to the relative location between the source point $\mathbf{p}$ and the field point $\mathbf{q}$. G is the simple Green function with a Rankine source and its image with respect to the bottom surface and the two lateral surfaces.

The higher-order boundary elements i.e. the eight-node quadratic isoparametric elements are used to discretize Eq. (10) at each time step, and then the following equation can be obtained

$$\begin{aligned}&\chi(\mathbf{p})\Phi_S(\mathbf{p})-\sum_{j=1}^{N_{e2}}\int_{-1}^{1}\int_{-1}^{1}\frac{\partial G(\mathbf{p},\mathbf{q})}{\partial n}\sum_{i=1}^{8}\Phi_{S(i)}h_i(\kappa,\eta)J(\kappa,\eta)d\kappa d\eta+\\&\sum_{j=1}^{N_{e1}}\int_{-1}^{1}\int_{-1}^{1}G(\mathbf{p},\mathbf{q})\sum_{i=1}^{8}\frac{\partial\Phi_{S(i)}}{\partial n}h_i(\kappa,\eta)J(\kappa,\eta)d\kappa d\eta=\\&+\sum_{j=1}^{N_{e1}}\int_{-1}^{1}\int_{-1}^{1}\frac{\partial G(\mathbf{p},\mathbf{q})}{\partial n}\sum_{i=1}^{8}\Phi_{R(i)}h_i(\kappa,\eta)J(\kappa,\eta)d\kappa d\eta-\sum_{j=1}^{N_{e2}}\int_{-1}^{1}\int_{-1}^{1}G(\mathbf{p},\mathbf{q})\sum_{i=1}^{8}\frac{\partial\Phi_{S(i)}}{\partial n}h_i(\kappa,\eta)J(\kappa,\eta)d\kappa d\eta\end{aligned} \tag{11}$$

where Ne_1 and Ne_2 denote the element number on the free surface and other surfaces, respectively; J is the Jacobian matrix; κ and η are the local intrinsic coordinate of each element surface; h is the quadratic shape function. The local integral of each element in Eq. (11) is solved using a 16-point Gauss-Legendre integral scheme if the source point is not the same as the field point. If the coordinate of the source point is identical to the field point, the transformation of a triangular polar coordinate [25], is used to assess the value.

Then Eq. (11) is assembled to obtain the final matrix equation

$$[\mathbf{A}]\begin{Bmatrix}\Phi_S\big|_{S_W+S_B^1+S_B^2}\\ \dfrac{\partial\Phi_S}{\partial n}\Big|_{S_F}\end{Bmatrix}=\{\mathbf{B}\} \tag{12}$$

where [**A**] is the influence coefficient matrix corresponding to the Green function and its derivatives, and {**B**} is the known vector.

2.3 Instantaneous wave loads

When fully nonlinear factors i.e. the instantaneous free surface and the wetted body surface are included in the numerical model, the general backward finite difference method cannot give the accurate solutions of the first term in Eq. (3) due to the numerical instability and divergence. In

this paper, some auxiliary functions [26 and 27] are introduced to solve the temporal derivative of the velocity potential i.e. $\partial\Phi^i / \partial t$

$$\frac{\partial \Phi^i}{\partial t} = \ddot{\xi}^i \cdot \psi_1^i + \psi_2^i \tag{13}$$

where ψ_1^i and ψ_2^i are auxiliary functions which satisfy the same governing equation with velocity potential, and are zero and unit normal vector on the free surface and body surface, respectively. Through solutions of these auxiliary functions using HOBEM and substituting Eq. (13) into (3), the hydrodynamic force $F^i{}_h$ can be expressed as

$$F_h^i = -\rho \ddot{\xi}^i \iint_{S_B^i} \psi_1 \cdot n_z^i dS - \rho \iint_{S_B^i} \left(\psi_2^i + \frac{1}{2} \left| \nabla \Phi^i \right|^2 + gz \right) \cdot n_z^i dS \tag{14}$$

Then, the motion equation i.e. Eq. (1) of each WEC can be re-written as

$$(M^i + c^i)\ddot{\xi}^i + b_{pto}^i \dot{\xi}^i + c_{pto}^i \xi^i = F_t^i \tag{15}$$

where

$$c^i = \rho \iint_{S_B^i} \psi_1 \cdot n_z^i dS \tag{16}$$

$$F_t^i = -\rho \iint_{S_B^m} \left(\psi_2^i + \frac{1}{2} \left| \nabla \Phi^i \right|^2 + gz \right) \cdot n_z^i dS \tag{17}$$

Eq. (15) is considered as the ordinary differential equations for the heave response ξ^i of i-th WEC, and is advanced in time using the fourth-order Runge-Kutta (RK4) scheme. For simplicity, Eq. (14) can be expressed in a general form

$$\ddot{\xi} = f(\Delta t, \xi, \dot{\xi}) \tag{18}$$

where Δt denotes time step. The displacement and velocity can be written as

$$\xi(t + \Delta t) = \xi(t) + \Delta t \dot{\xi}(t) + \Delta t (G_1 + G_2 + G_3)/6 \tag{19}$$

$$\dot{\xi}(t + \Delta t) = \dot{\xi}(t) + (G_1 + 2G_2 + 2G_3 + G_4)/6 \tag{20}$$

where intermediate functions G_1, G_2, G_3 and G_4 is defined as

$$G_1 = \Delta t \cdot f(t, \xi(t), \dot{\xi}(t)) \tag{21}$$

$$G_2 = \Delta t \cdot f\left(t + \frac{\Delta t}{2}, \xi(t) + \frac{\Delta t \cdot \dot{\xi}(t)}{2}, \dot{\xi}(t) + \frac{G_1}{2}\right) \tag{22}$$

$$G_3 = \Delta t \cdot f\left(t + \frac{\Delta t}{2}, \xi(t) + \frac{\Delta t \cdot \dot{\xi}(t)}{2} + \frac{\Delta t \cdot G_1}{4}, \dot{\xi}(t) + \frac{G_2}{2}\right) \tag{23}$$

$$G_4 = \Delta t \cdot f\left(t + \Delta t, \xi(t) + \Delta t \cdot \dot{\xi}(t) + \frac{\Delta t \cdot G_2}{2}, \dot{\xi}(t) + G_3\right) \tag{24}$$

The detailed solution process is described as follows. At the initial time, the flow function

$f(t,\xi(t),\dot{\xi}(t))$ is obtained using the given initial displacement and velocity. The dynamic analysis starts from a static equilibrium location, and thus G_1 can be given according Eq. (21). And then the displacement and velocity at next iterative step can be updated, and G_2 are also calculated according to Eq. (22). Similarly, G_3 and G_4 are obtained using Eqs. (23) and (24), and thus the displacement and velocity at next time step can be computed using Eqs. (19) and (20).Then, the calculations for the next time step is processed, including the discretization of water integral equation and the solutions of motion equation.

2.4 Energy extraction and transmitted coefficient

The wave resonance in the multi-moonpool affects the hydrodynamic performance of each WEC device, which may enhance the highest possible efficiency in open water. In this paper, the average generated power E^i_p at wave period T produced by the i-th WEC is derived as

$$E_p^i = \frac{1}{mT}\int_t^{t+mT} F_h^i \dot{\xi}^i dt = \frac{b_{\text{pto}}}{mT}\int_t^{t+mT} \left(\dot{\xi}^i\right)^2 dt \tag{25}$$

For an array of dual WEC devices, the total generated power E_p can be expressed as

$$E_p = \sum_{i=1}^{2} E_p^i \tag{26}$$

In order to decompose the incident waves and reflected waves of the multi-purpose platform, two wave gauges are installed at 10 m and 12 m from the front of the structure using the traditional two-point method [28]. Another two-wave gauges are placed at 11 m and 35 m from the rear of the structure, respectively, to obtain the transmitted wave height and examine the wave absorption ability of the damping lay at the end. The reflected coefficient K_r and transmitted coefficient K_t are calculated as

$$K_r = \frac{H_r}{H_I} \tag{27}$$

$$K_t = \frac{H_t}{H_I} \tag{28}$$

where H_r, H_t, and H_I are the wave heights of the reflected, transmitted and incident waves, respectively.

To quantify the mutual effects between the floating breakwater and the WECs, the mean interaction factor q^E_{mean} for wave energy extraction is introduced. It is regarded as the ratio of the total wave energy of this multi-purpose platform and the dual isolated WECs, it is defined as

$$q^E_{\text{mean}} = \frac{E_p}{E_{\text{isolated}}} \tag{29}$$

where E_{isolated} is the average generated power of the dual isolated WECs, and is obtained by simulating the hydrodynamic performance of dual isolated WECs in the absence of floating breakwater. When $q_{\text{mean}}>1$, the moonpool effect is known as a positive interaction. This means that the extracted wave energy of this platform is higher than the one of the isolated WECs. Conversely,

when q_{mean}<1, the moonpool effect is known as a destructive interaction.

The interaction factors q^r_{mean} and q^t_{mean} for the wave attenuation are further defined as

$$q^r_{\text{mean}} = \frac{K_r}{K_r^{\text{isolated}}} \tag{30}$$

$$q^t_{\text{mean}} = \frac{K_t}{K_t^{\text{isolated}}} \tag{31}$$

where K_r^{isolated} and K_t^{isolated} are the reflected and transmitted coefficients of the isolated floating breakwater, respectively.

Based on the conservation of energy, the incident wave energy E_w within one wave period T is described by

$$E_w = \frac{2R_w^i \lambda}{T^2} \int_0^T \int_{-l}^{\eta_1(0,t)} \Phi_{\text{Ix}} \cdot \Phi_{\text{Ix}} dz dt \tag{32}$$

where λ is the wavelength, and R^i_w is the structural radius of i-th WEC. Therefore, the capture efficiency R of the array of the WECs can be determined as the ratio of the extracted power to the wave power

$$R = \frac{E_p}{E_w} \tag{33}$$

3. Convergence study and comparison

3.1 Convergence study

A multi-purpose platform of a floating breakwater and an array of dual WECs is chosen to conduct the mesh and time convergent tests. The breakwater having the length L=15 m × width B=20 m consists of two 8 m (diameter $2R_f$) × 15 m (length L) cylinders which are connected using tree bulkheads with dimensions 8 m (height h_f) × 20 m (width B). The breakwater has the same size as the moonpools inside. Two cylindrical WECs with dimensions 2 m (diameter $2R^i_w$) × 4 m (height h^i_w) are installed inside each moonpool, respectively. The drafts of the breakwater and WECs are d_f=4 m and d^i_w=3 m, respectively. In the numerical simulation, the mechanical coefficients of the PTO system are set as b_{pto}=3500 N•s/m, and c_{pto}=0. The above geometrical dimensions are based on the prototype design of the moonpool-type floating breakwater which has been deployed in South China Sea [29]. The whole computational domain is taken as 6λ (length) ×20 m (width) ×30 m (water depth). Three mesh schemes are adopted. For mesh a, on the free surface, the element size is defined as $\Delta x=\Delta y=\lambda/10$. Five layers are employed along the truncated boundary surface at the far-field. On the body surface, 8 elements and 7 elements are specified along with the vertical directions of the breakwater and WECs. The breakwater is divided into 15 and 20 elements along the length and width direction, and 10 elements are used in the radial direction of each WEC. Mesh b is the finer mesh scheme, in which, the element number is doubled compared to Mesh a, on the free surface and body surface. Mesh c is the coarser mesh scheme, in which the element number is two-thirds of that of Mesh a on the free surface and body surface. Fig. 4 gives the heaving response of each WEC with different meshes for the incident wave height H_I=3 m and incident wave period 5 s. Here, the time step $dt=T/60$ is adopted. It can

be seen that each WEC oscillates with larger amplitude in the downward direction than in the upward direction, which is because the initial mechanical loads generated by PTO system leads to the deviation of equilibrium position of the motion. This also found experimentally by Ning et al. [10] and numerically by Liu et al. [24]. Although the phase of the motion responses for three meshes is almost identical, the negative heaving amplitude of each WEC for Mesh c is larger by 3% than the one for Mesh a and Mesh b. And the amplitude difference of Mesh a and Mesh b is less than 3%. Furthermore, the temporal convergent tests are performed with three-time steps: $dt=T/100$, $dt=T/60$, and $dt=T/30$, as shown in Fig. 5. The results indicate that the intermediate time step $dt=T/60$ can give desirable solutions. Therefore, Mesh a and time step $dt=T/60$ are used in the following simulation.

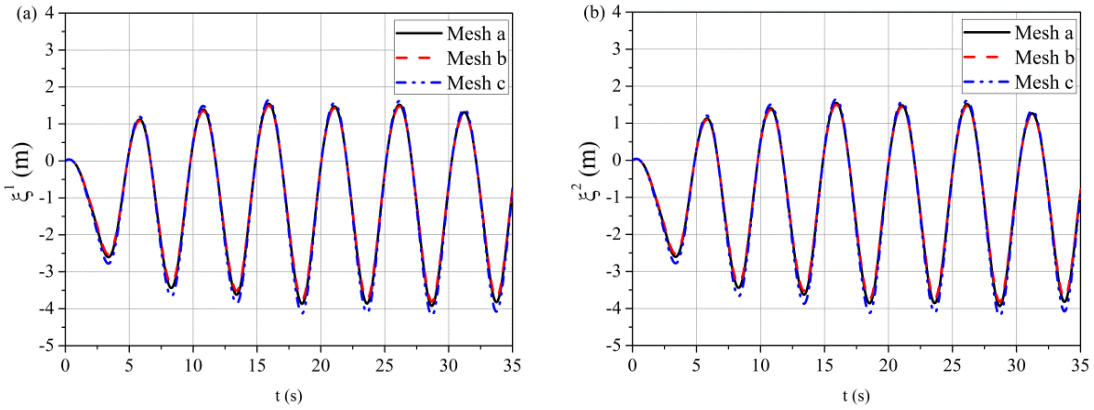

Fig. 4. Convergence of heaving motion with different meshes for (a) 1-th WEC and (b) 2-th WEC with incident waves with H_I=3 m and T=5 s

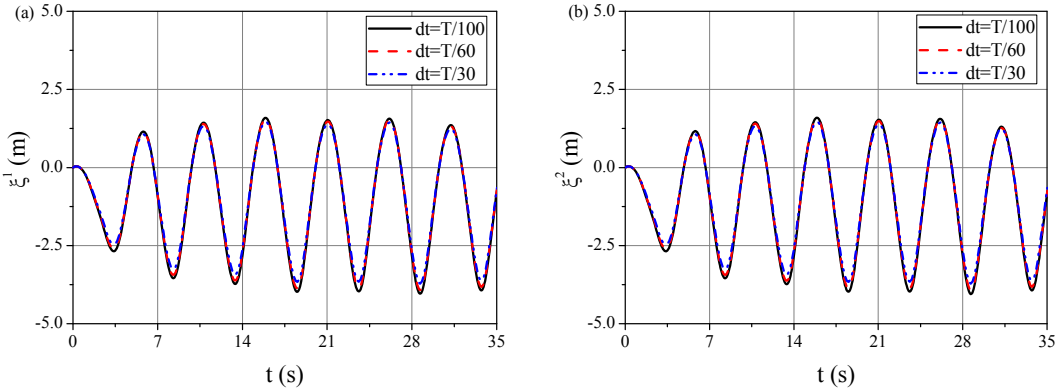

Fig. 5. Convergence of heaving motion with different time steps for (a) 1-th WEC and (b) 2-th WEC with incident waves with H_I=3 m and T=5 s

Next, the sensitivity of the reflection and transmission coefficients with respect to the coordinates of wave gauges is examined in Fig. 6 with geometric and wave parameters being the same as those in Fig. 5, because the gap between the lateral wall of the NWT and the structure edge would induce some transverse standing waves which affect the accuracy of the two-point method. Here, the x-axis in Fig. 6 (a) and (b) denotes the distance from the front and rear of the structure, respectively. It can be seen that at small distance, the reflection and transmission coefficients oscillates with distance. After the distance increase to certain values i.e. 10 m from the front of the structure and 11 m from the rear of the structure, the effect of the gap between tank wall and structure on the wave attenuation capacity of the floating breakwater gradually vanish, which leads to insignificant variation of the reflection and transmission coefficients, i.e. K_R=0.41

and K_t=0.70. Therefore, in this paper, two wave gauges are installed at 10 m and 12 m from the front of the structure to decompose the incident waves and reflected waves. Another one wave gauge is placed at 11 m from the rear of the structure to measure the transmitted wave surface elevation.

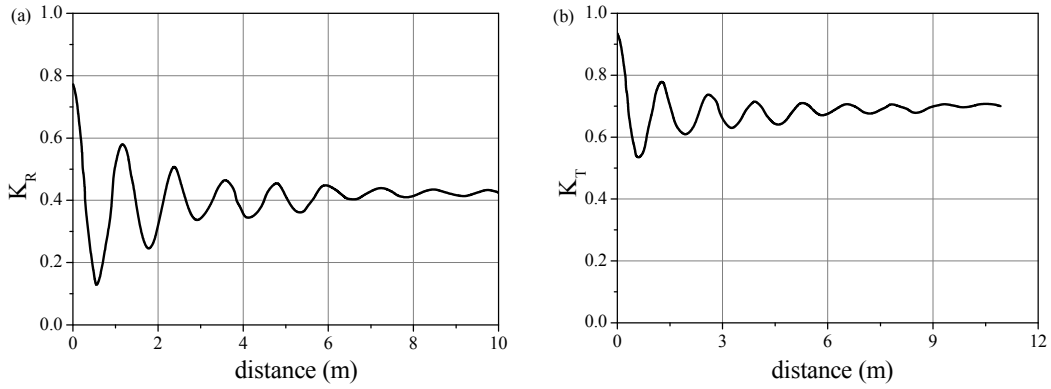

Fig. 6. Sensitivity of (a) the reflection coefficient and (b) the transmission coefficient with respect to the distance from the front or the rear of the structure

3.2 Comparison

To verify the accuracy of the present fully nonlinear model, an integrated system of a semi-submersible triangular platform and an array of 3×3×3 cylindrical WECs by Hu et al. [30], is considered with the draft d=3.22 m, the radius r=3.22 m, the distance between the WECs L_1=10.68 m and the distance between the platform and the WEC L_2=12.18 m. The platform is fixed and each WEC only has heaving motion. Fig. 7 gives the mesh of the integrated system, in which 130 elements are used on each WEC and 2800 elements on the foundation following the convergent test. The incident wave height is 0.84 m. Fig. 8 shows the variation of the total generated power E_p and the mean interaction factor q^E_{mean} for the array of WECs with the wave frequency under the optimal PTO damping b^i_{opt} can be obtained from

$$b^i_{opt} = \sqrt{\frac{((M^i + a^i_z)\omega^2 - (c^i_{pto} + c^i_z))^2}{\omega^2} + b^i_z} \tag{34}$$

where a^i_z, b^i_z and c^i_z are the added mass coefficient, radiation damping coefficient, and restoring force coefficient of the i-th WEC, respectively. The comparison against the numerical results obtained by linear solutions from Hu et al. [30] is also given in the figures. The nonlinear factors i.e. the large deformation of the free water surface and instantaneous motion of the body, leads to a small difference between the present fully nonlinear model and the potential linear model [27], especially for the total generated power E_p near the resonant frequency $\omega_n = 1.25$. Overall, the present model correlates well with the published results, which indicates enough accuracy for simulating the hydrodynamic behavior of the multi-purpose platform in this paper.

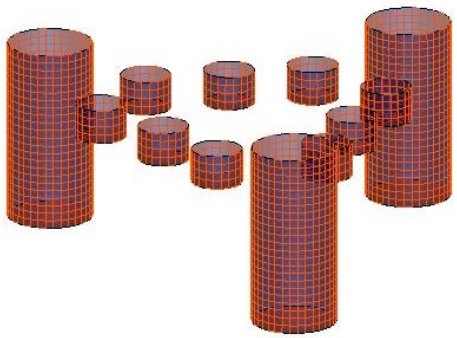

Fig. 7. Meshes on body surfaces

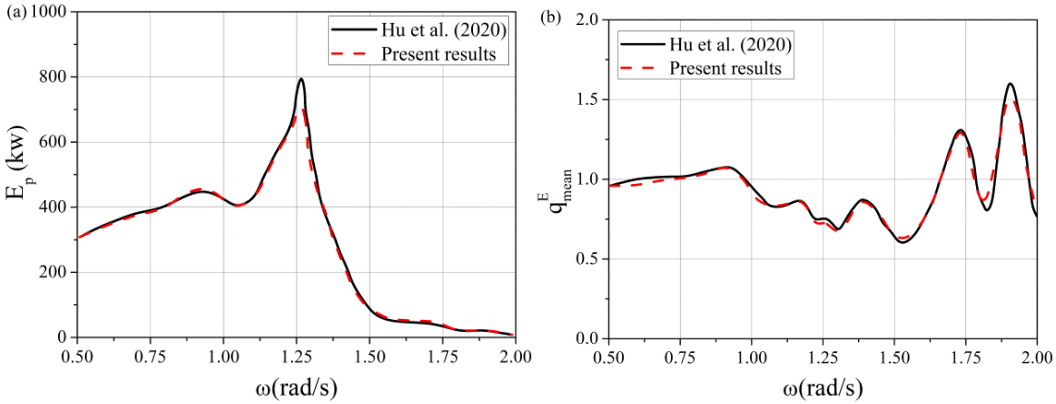

Fig. 8. Comparison of (a) the total generated power and (b) the mean interaction factor with the potential linear results in Hu et al. [30]

To further validate the present numerical method, the numerical solution of a breakwater-type WEC consisting of a front heaving WEC and a rear fixed pontoon, is compared to the published experimental results conducted by Zhao and Ning [31] and the linear analytic soultions by Ning et al. [32]. The geometric parameters are identical between two pontoons with draft d_f=d_w=0.125 m, width B=0.6 m, length L=2 m, and the gap between pontoons s=0.2 m. The tested water depth is d=1 m, and the various PTO damping foces are described in Ref. [31]. The wave frequency range ω=3.2 rad/s-5.6 rad/s is considered in the experiment. Fig. 9 (a)-(d) shows the comparison of the numerical, analytic and experimental heaving amplitude ξ_0, capture efficiency R, reflection coefficient K_R and transmission coefficient K_T. It can be seen that the general shapes of curves correlate well with each other. In addition, the nonlinear results by the proposed model are in better agreement with the experimental results than the linear solutions of Ning et al. [32]. This is because in the linear model, the body wetted-surface is alwalys constant and the free surface conditions are established based on the clam water surface. However, in the fully nonlinear model, the free surface and wetted surface are updated continuously as the floating body moves. The slight discrepancy between numerial and experimental results can be attributed to the possibly un-captured physics (such as the friction effect between floater and vertical pile).

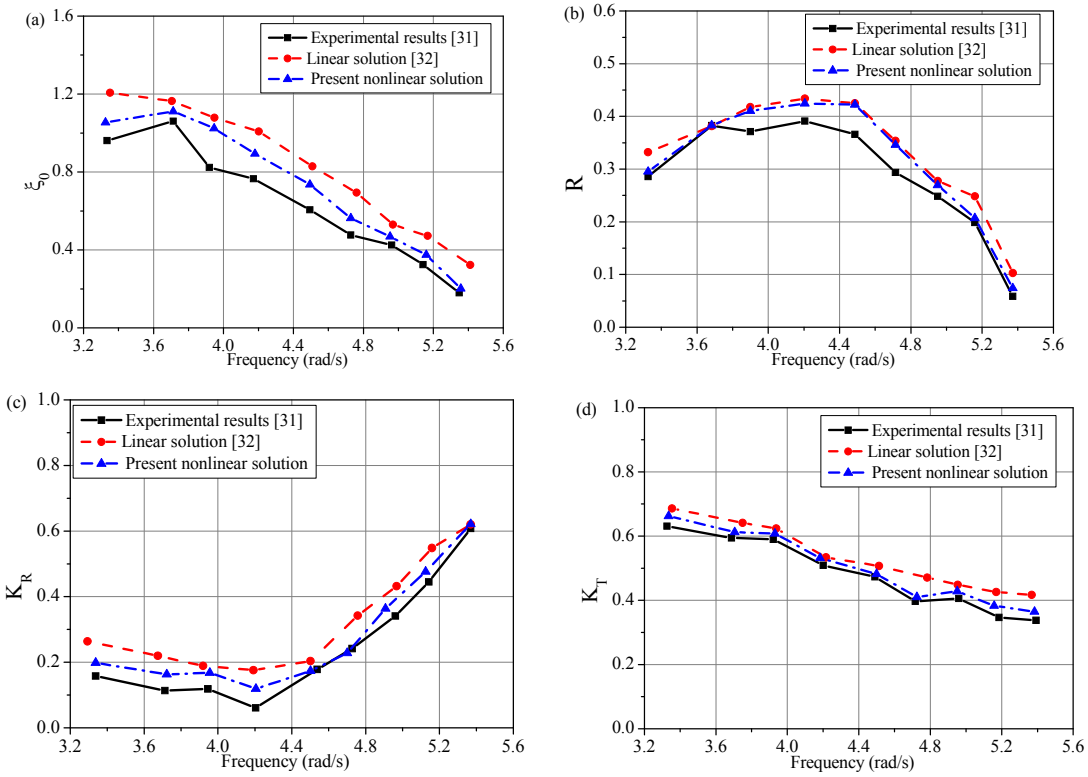

Fig. 9. Comparison of (a) the WEC-heaving amplitude, (b) the capture efficiency, (c) the reflection coefficient and (d) the transmitted coefficient with the experimental results in Zhao and Ning [31] and the linear solutions in Ning et al. [32]

4. Numerical results

In this section, the performance analysis of the multi-purpose floating platform is discussed by comparing it to a single breakwater and isolated dual WECs. In addition, the effects of designed parameters i.e. the geometric size of WECs, PTO damping coefficient, moonpool configuration, wave direction, and wave amplitude, are emphatically examined. For convenience, the fluid density ρ, the water depth h, and the acceleration g of gravity are used for non-dimensionalize in the following discussion. Thus, the non-dimensional parameters including motion response of each WEC ξ^i, WEC diameter $2R^i_w$, wave period T, wave height H_I, PTO damping b_{pto}, PTO stiffness c_{pto} and pressure p are calculated based on $\xi^i=(\xi^i)_{\text{dimensional}}/h$, $2R^i_w=(2R^i_w)_{\text{dimensional}}/h$, $H_I=(H_I)_{\text{dimensional}}/h$, $T=(T)_{\text{dimensional}}\sqrt{g/h}$, $b_{pto}=(b_{pto})_{\text{dimensional}}/\sqrt{\rho^2 gh^5}$, $c_{pto}=(c_{pto})_{\text{dimensional}}/(\rho gh^2)$, and $p=(p)_{\text{dimensional}}/(\rho gh)$.

4.1 Performance analysis

To compare the hydrodynamic performance of the multi-purpose floating platform to that of the single breakwater and isolated dual array WECs, numerical simulations are carried out with different wave periods and constants. The other parameters are the same as Section 3.1. Fig. 6 shows the motion amplitude ξ^i_0, the total average generated power E_p, and the capture efficiency R as functions of non-dimensional wave period T. The motion amplitude ξ^i_0 is almost identical for different WEC in the same layout over the whole tested wave period due to the wave incident direction. It can be seen that the presence of the floating breakwater cannot affect the natural period T_n of the WECs (about T_n=2.8) and the curve shapes of the motion response, the extracted

power, and the capture efficiency. The results are not sensitive to with and without floating breakwater in the short wave region (T<2.8), while those for the multi-purpose floating platform are significantly increased compared to the WECs-only cases in the longwave region (T>2.8). For example, the maximum increasing ratios for $\bar{\xi}_0$, E_p, and R, are 30.01%, 77.61%, and 77.61%, respectively. The reason is that more surface waves are transmitted through the seaward side and into the moonpools with increasing incident wave period, and thus, the internal fluid motion can be further strengthened induced by the piston and the sloshing responses. Fig.6 (c) reveals that the maximum efficiency improvement occurs at a wave period T=3.4. This indicates that the rate of the free surface elevation changing in the moonpools is the highest at T=3.4, which is near the natural period of the internal fluid motion.

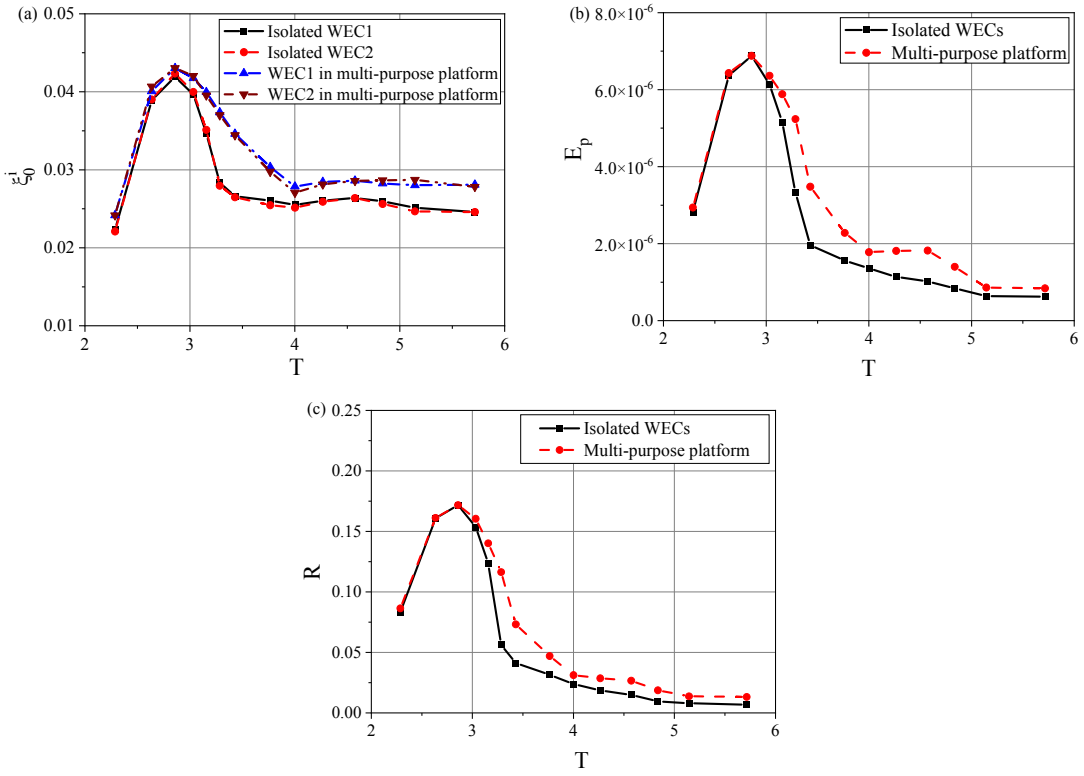

Fig. 10. Variations of motion amplitude $\bar{\xi}_0$, the total average generated power E_p, and the capture efficiency R versus non-dimensional wave period T for different models

Furthermore, the comparison of the wave attenuating capacity represented by the wave reflection coefficient K_R and transmission coefficient K_T for the multi-purpose platform and the isolated floating breakwater, is given in Fig. 11 (a)-(b). The reflection coefficient K_R of the multi-purpose platform is larger than the one of the isolated breakwater, especially near the natural period of the WECs. At a larger wave period, the difference in K_R between the two models is small. The transmission coefficient K_T depicted in Fig. 11 (b) for both models generally increases with the wave period, indicating that longer waves are more easily transmitted over the floating breakwater. K_T for the multi-purpose platform is obviously reduced compared with that of the isolated breakwater in the short wave region, with the largest reduction ratio of 8.19% near T=2.8. This is because, deploying dual array WECs in the moonpools of the floating breakwater can lead to the energy transformation from the fluid to the WEC, which reduces the transmission wave energy. This is especially obvious at periods near to the one for maximum capture efficiency as shown in Fig. 10(c). With increasing wave period, K_T for different models gradually merges

together because the draft of the breakwater is smaller than the wavelength, which is the determining factor for wave attenuating capacity.

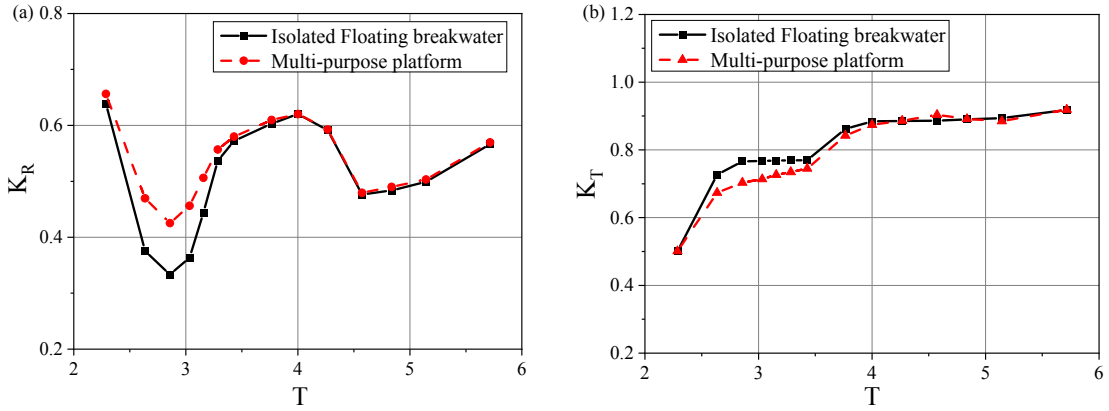

Fig. 11. Comparison of wave reflection coefficient K_R and transmission coefficient K_T of the multi-purpose platform with isolated floating breakwater

4.2 Effect of WEC diameter $2R^i_w$

The multi-purpose floating platform with three different WEC diameters $2R^i_w$=0.033, 0.050, and 0.067 was selected in order to examine the effect of the WEC horizontal size on platform performance. Fig. 12 gives the variation of the motion amplitude ξ^i_0, the total average generated power E_p, and the capture efficiency R against wave period T. As shown in Fig. 12 (a) and (b), both the heaving motion response and energy extraction increases with increasing WEC diameter. This feature is caused by the increased water-plane area of WECs. The larger water-plane area leads to larger heaving hydrodynamic loads. In addition, the resonant period decreases with increasing WEC diameters. This is due to the restoring stiffness $\rho g A_W$ of WEC increasing with the WEC diameter. The approximated resonant period formula by Zhang et al. [16] for a heaving WEC is obtained as follows:

$$T_n = 2\pi\sqrt{\frac{\rho g A_W d_w + a_z}{c_{pto} + \rho g A_W}} \tag{27}$$

Here, A_w denotes the water-plane area and c_{pto}=0. Thus, the dependence of the resonant period on the WEC diameter can be found in Eq. (27). Fig. 12 (c) reveals that the capture efficiency of the WECs increases near the resonant period region when the WEC diameter increases from $2R^i_w$ =0.033 to 0.050. After the WEC diameter increases to $2R^i_w$ =0.050, the increased incident wave energy is considered to be the average generated power, which results in an insignificant variation of capture efficiency.

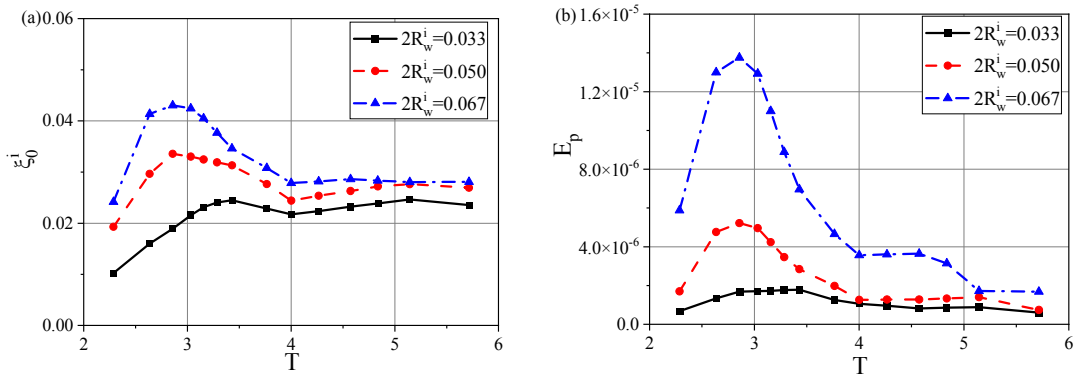

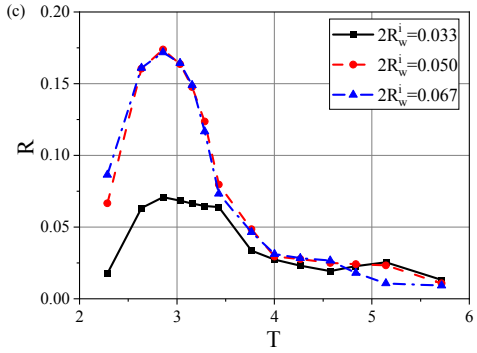

Fig. 12. Variations of motion amplitude ξ_0, the total average generated power E_p, and the capture efficiency R versus non-dimensional wave period T for different WEC diameters

Fig. 13 gives the variation of the wave reflection coefficient K_R and transmission coefficient K_T against the wave period T. As shown in this figure, the effect of the WEC diameter $2R^i_w$ on the wave attenuating capacity is more complicated than the one on the energy extraction of the multi-purpose floating platform. K_R near-resonant period of WECs increases with increasing WEC diameter due to the increase of the effective seaward area induced by the WEC heaving resonance as shown in Fig. 13 (a). But K_R for $2R^i_w$ =0.050 is the largest among the three WEC diameters in the wave period region $4.2>T>3.8$ and is the smallest in the wave period region $T>4.2$, due to the fluid resonance in the moonpools. K_T is almost unchanged when T is smaller than 3.5, it firstly decreases with increasing WEC diameter when T is larger than 3.5 and then increases after reaching the minimum value. Such behavior indicates that the size design with WECs should be done with rigorous analysis for practical wave conditions. For example, in a particular case, the WEC design with $2R^i_w$=0.050 can reach a desirable level between the wave energy extraction and wave transmission.

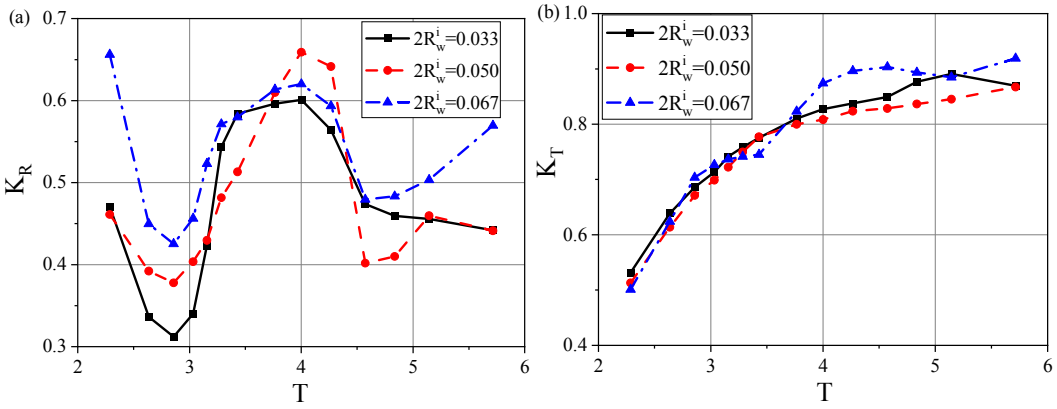

Fig. 13. Variations of wave reflection coefficient K_R and transmission coefficient K_T versus non-dimensional wave period T for different WEC diameters

The mean interaction factors q^E_{mean}, q^r_{mean}, and q^t_{mean} obtained by Eq. (21)-(23), are shown in Fig. 14 to investigate the moonpool effect on wave energy extraction and wave attenuation. Fig. 14 (a) reveals that the fluid resonance in the moonpools has a benefic effect on the wave energy extraction for all WEC diameters. The variation trends of q^E_{mean} with wave period are similar, but the occurring position of the maximum or minimum q^E_{mean} is different for different WEC diameters. Compared to the isolated dual array WECs, the moonpool effect is more obvious for the WEC diameter $2R^i_w$=0.050 near the resonant period region of the WECs. At a larger wave period, the increase of WEC diameter can enhance the moonpool effect on the wave energy

extraction. Fig. 14 (b) indicates that q^r_{mean} is almost lower than 1 in the whole tested period range for the WEC diameter $2R^i_w$=0.033, which may be because the smaller WEC diameter induces more energy dissipation. When the WEC diameter increases to $2R^i_w$=0.067, q^r_{mean} is almost equal to 1 in the long wave region (T>3.5). This means that the effect of the WEC motion on wave reflection is very small, as the WEC motion is relatively smaller than the incident wavelength in these periods. Fig. 14 (c) depicts that q^t_{mean} is larger than 1.0 at some wave periods, but is generally smaller than 1.0. This indicates that the installation of the array WECs in the moonpools is usually positive for the total wave attenuation of the wave field. Besides, when the WEC diameter is $2R^i_w$=0.050, the multi-purpose floating platform has a significant enhancement of wave attenuation in the long wave region (T>4) compared to the isolated breakwater, which extends the wave period range of practical engineering applications.

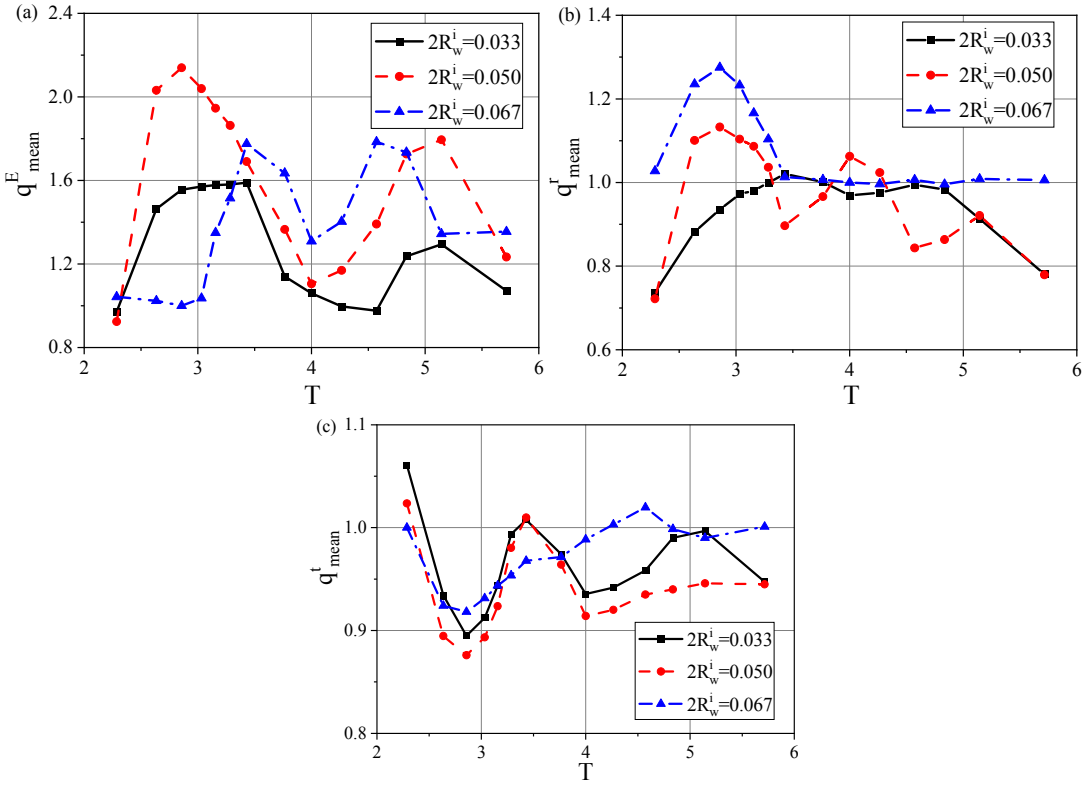

Fig. 14. Variations of mean interaction factors q^E_{mean}, q^r_{mean}, and q^t_{mean} versus non-dimensional wave period T for different WEC diameters

4.3 Effect of nonlinear factors

In linear wave theory, the response amplitude ξ^i_0, and the total average generated power E_p are approximately linearly proportional to H and H^2, respectively, while the capture efficiency R is independent of H according to Eq. (25). However, when some nonlinear factors are considered, such as body motion with large amplitude and wave nonlinearity, some interesting features appear. The motion of the WECs is resisted by the PTO mechanical loads i.e. PTO damping b_{pto}, and the wave nonlinearity is directly related to the incident wave height H_I. Therefore, Fig. 15 shows the variation of the response amplitude ξ^i_0/H_I, the total average generated power E_p/H_I^2, and the capture efficiency R with b_{pto} for three different incident wave heights H_I =0.033, 0.1 and 0.167 and wave period T=2.8. Here, the WEC diameter is set as $2R^i_w$ =0.067 and the other parameter are the same as Fig. 14. It can be seen that the heaving motion of each WEC decreases with increasing b_{pto}, while the energy extraction firstly increases with b_{pto}, and reaches the maximum at optimal

damping, then decreases as b_{pto} further increases. The reason is that the motion of the WECs is inversely proportional to the PTO damping, and the energy extraction is proportional to both PTO damping and WEC motions. All results are reduced with increasing incident wave height, which is in contradiction with the previously described linear theory. This indicates that when wave nonlinearity becomes more and more prominent, the capture efficiency of the multi-purpose platform is mitigated. For example, the maximum efficiency for H_I =0.033, 0.1 and 0.167, are 0.3, 0.2 and 0.1, respectively. In addition, when the incident wave height is small i.e. H_I =0.033, the optimal PTO damping is equal to 5×10^{-4}, which is almost identical to Eq. (26). As the incident wave height increases, the optimal PTO damping gradually decreases and occurs at $b_{pto}=5\times10^{-4}$, 4×10^{-4}, and 3.5×10^{-4} for $H_I = 0.1$ and 0.167, respectively.

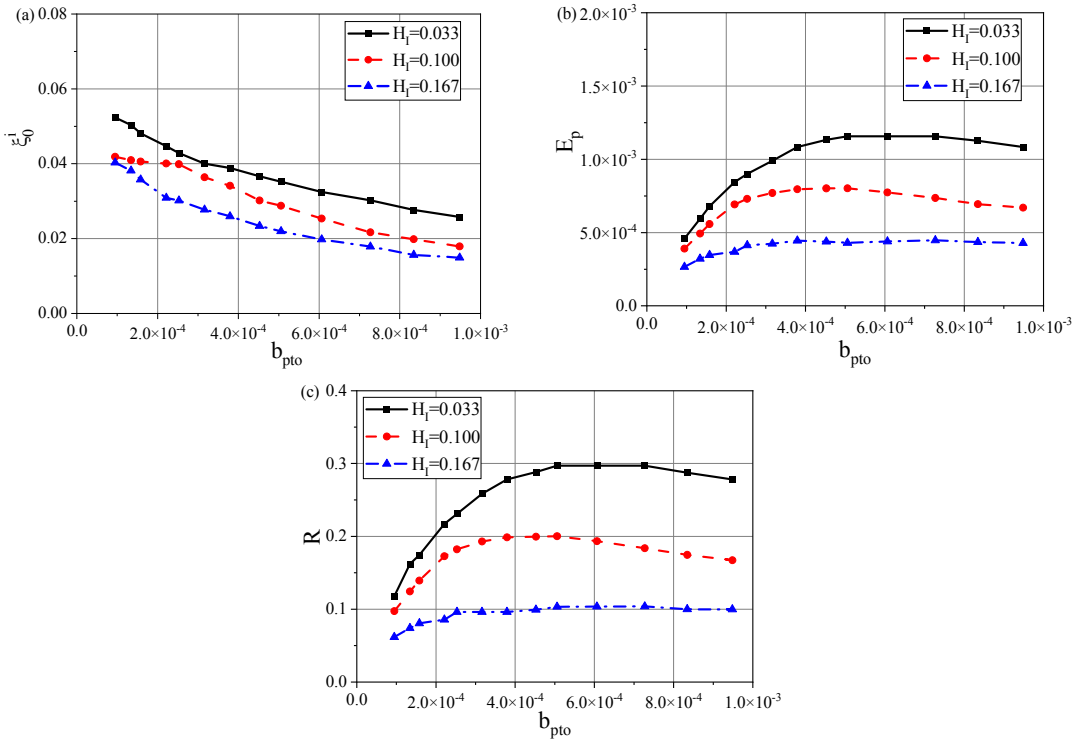

Fig. 15. Variations of motion amplitude ξ_0/H_I, the total average generated power E_p/H_I^2, and the capture efficiency R versus non-dimensional PTO damping b_{pto} for different incident wave heights

Fig. 16 shows the attenuating capacity of the multi-purpose platform for different wave heights and PTO damping coefficients. From Fig. 16(a), it can be seen that when the incident wave height increases from H_I =0.033 to 0.1, the reflection coefficient increases significantly due to the increase of the structural projected area in the direction normal to incident wavelength called as effective seaward area. However, when the incident wave height is larger than 0.1, the reflection is practically unchanged, which means that the effective seaward area reaches a maximum in this particular case. For fixed incident wave height, the reflection coefficient for different PTO damping corresponds to almost the same value. This indicates that b_{pto} has a weak effect on the reflected feature of the multi-purpose platform, and the effective seaward area is a dominant factor. The total transmission coefficient in Fig. 16 (b) for H_I=0.033 and 0.1 increases with increasing b_{pto}, but that for H_I=0.167 follows a completely opposite trend. Also, at large PTO damping (b_{pto} >4×10^{-4}), the transmission coefficient decreases with increasing incident wave height. Accordingly, more wave energy is absorbed as both incident wave height and PTO damping increase because of a stronger nonlinear motion of the internal fluid in the moonpools. This further

reveals that the presence of the moonpools plays an important role in reducing the transmitted wave height downstream the multi-purpose platform.

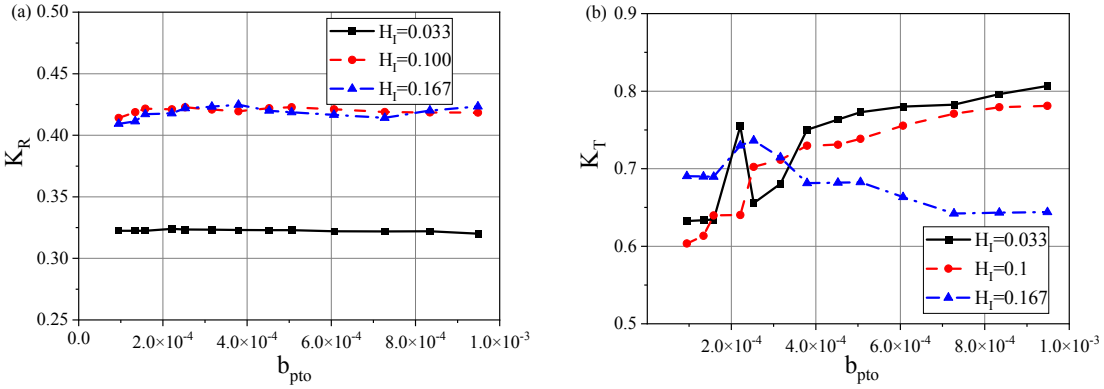

Fig. 16. Variations of wave reflection coefficient K_R and transmission coefficient K_T versus non-dimensional PTO damping b_{pto} for different incident wave heights

To further illustrate the relationship between the wave nonlinearity and the wave energy extraction, Fig. 17 (a)-(c) shows the dependence of the response amplitude ξ^1_0/H_I, the total average generated power E_p/H_I^2, and the capture efficiency R on wave peirod for three different incident wave heights H_I =0.033, 0.1 and 0.167 with b_{pto}=2.2×10^{-4}. It can be observed that the variation trend of all resultant curves including WEC motion and energy extraction with wave period are almost identical among different wave heights, but results decrease with increasing wave height, especially near maximum values. The maximum capture efficiency for H_I=0.033, 0.1 and 0.167 are 21.71%, 17.18% and 9.13%, repectively. However, the occurring wave period of the maximum wave energy extraction is approximately unchanged and occurs at about T=2.85. This suggests that the WEC configuration designed for a particular range of wave periods and small wave heights should also be adequate for large wave heights.

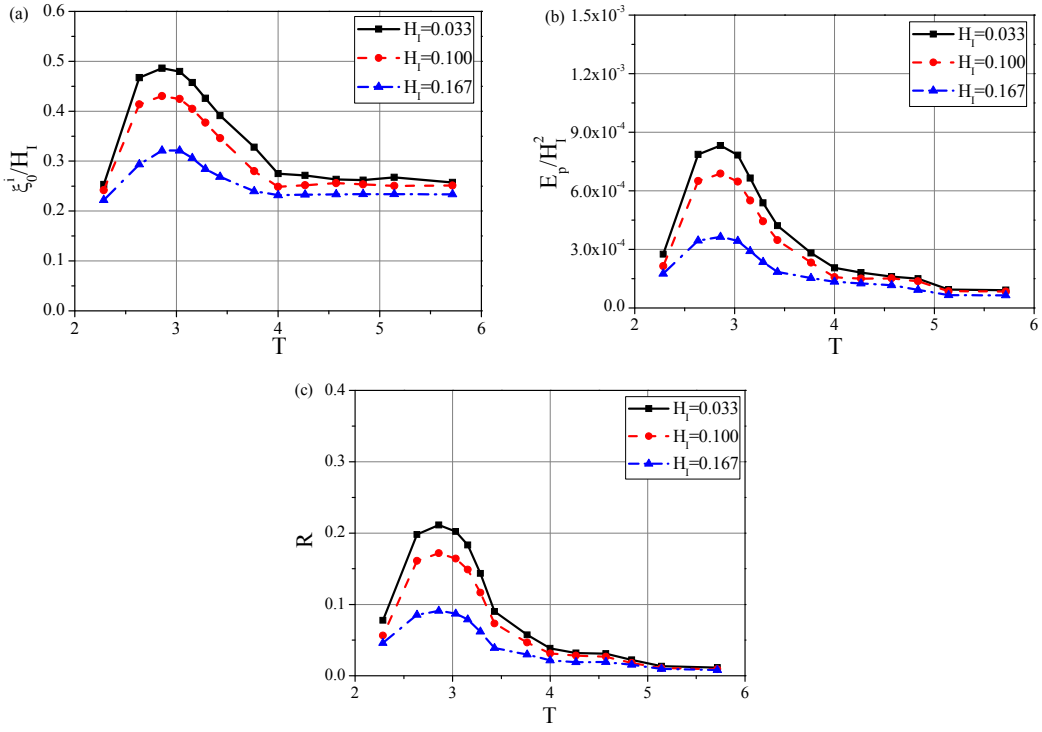

Fig. 17. Variations of motion amplitude ξ^1_0/H_I, the total average generated power E_p/H_I^2, and the capture efficiency

R versus wave period T for different incident wave heights

4.4 Effect of moonpool size

To study the effect of the moonpool size on the hydrodynamic performance of the multi-purpose platform, numerical simulations are conducted for three different moonpool sizes, as shown in Fig. 18. Here, Cases 1 to 3 denote that the width ratios of the left and right moonpools are 1:3, 1:2, and 1:1, respectively. Each WEC with $2R^i_w$=0.033 is installed at the moonpool center. Fig. 19 gives the response amplitude ξ_0 of each WEC for three cases with H_I=0.1 and b_{pto}=5×10^{-4}. The heaving response of WEC decreases with increasing moonpool length in the short wave region (T<4) but increases in the long wave region (T>4), implying that narrow moonpool boosts the motion of internal waves with high frequency and reduces that with low frequency. What's more, the resonant period increases with increasing moonpool length. The is due to the increase in water mass in the moonpool. The total average generated power and the capture efficiency are given in Fig. 20. It can be seen that the maximum amplitudes of both the average generated power E_p and the capture efficiency R decrease for the more unequal layout of moonpools, but the wave energy extraction in the short wave region (T<3.5) is improved by the unequal moonpools. This is reasonable since the thinner moonpool can lead to a stronger oscillation of the water column in the gap. Compared to equal moonpools i.e. Case 3, both E_p and R decrease in the long wave region (T>3.5) for unequal moonpools. In a practical wave farm, the most typical floating breakwater system is assembled by an array of multiple floating modules connected to each other using flexible connectors along their longitudinal direction. Thus, it is recommended that a different number of equal moonpools is deployed in different modules to broaden the effective bandwidth of the wave energy extraction. In addition, the wave period corresponding to the maximum amplitude also decreases for the more unequal layout of moonpools. This indicates that for the unequal layout of moonpools, the thinner moonpool plays a dominant role in wave energy extraction compared to the fatter moonpool.

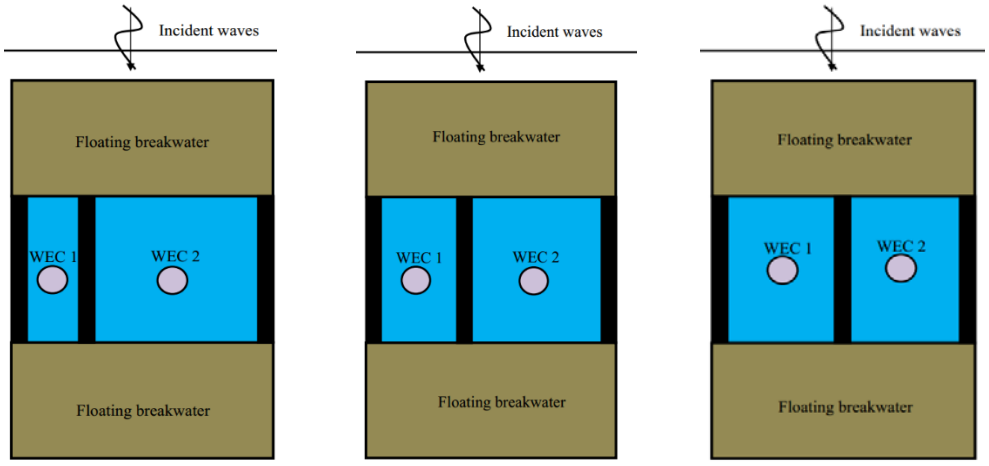

(a) Case 1 (b) Case 2 (c) Case 3

Fig. 18. Multi-purpose platform with three different moonpool sizes

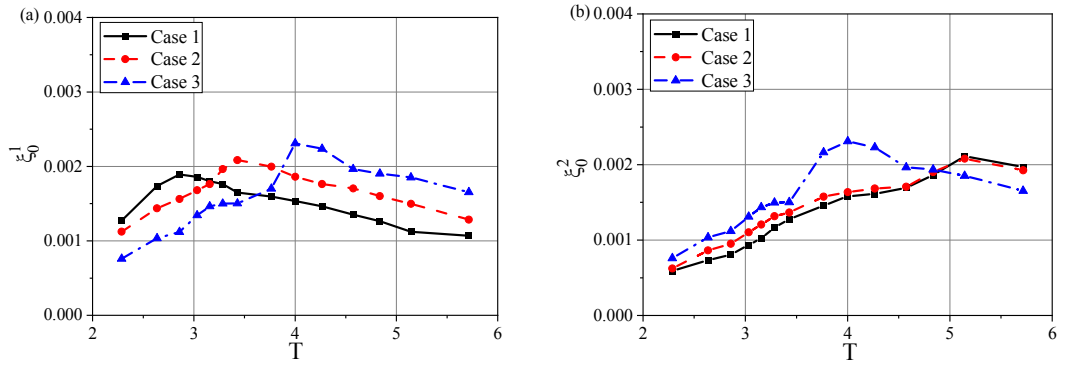

Fig. 19. Variations of motion amplitude ξ_0^j versus non-dimensional wave period T for different moonpool sizes

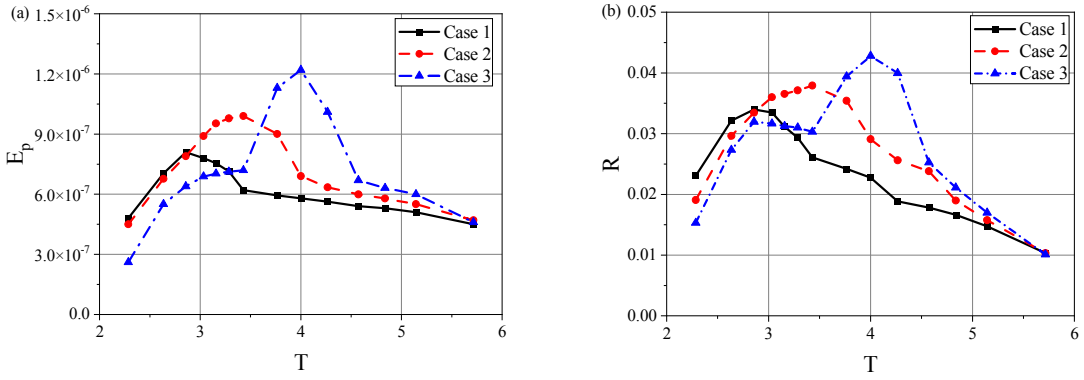

Fig. 20. Variations of (a) the total average generated power E_p and (b) the capture efficiency R versus non-dimensional wave period T for different moonpool sizes

The variation of the reflection coefficient and the transmission coefficient with wave period for different moonpool layouts is shown in Fig. 21. From Fig. 21 (a), it can be found that the reflection coefficient increases for the more unequal layout of moonpools in the short wave region (T<4), whereas it is not sensitive to the change of moonpool size in the long wave region (T>4). This is consistent with short waves showing lower wave transmission capacity, which can be reflected advantageously by the wall-side surfaces of front and back pontoons. The transmission coefficient in Fig. 21 (b) for unequal moonpool layout in the wave period range of 2<T<3.5 is smaller than that for equal moonpool layout, but vice versa in the wave period range of 3.5<T<4.5. This is reasonable since the resonant response of the WEC in thinner moonpools for Cases 1 and 2 occurs at the wave period range of 2<T<3.5, but that in equal moonpools for Case 3 occurs at the wave period range of 3.5<T<4.5 as indicated in Fig. 21(a). This leads to more energy transforming from waves to WEC motions. Furthermore, the transmission coefficient in the longwave region i.e. T>4.5 decreases for unequal moonpool layouts, which is because the motion of WEC in the fatter moonpools for Cases 1 and 2 can be amplified as shown in Fig. 21(b).

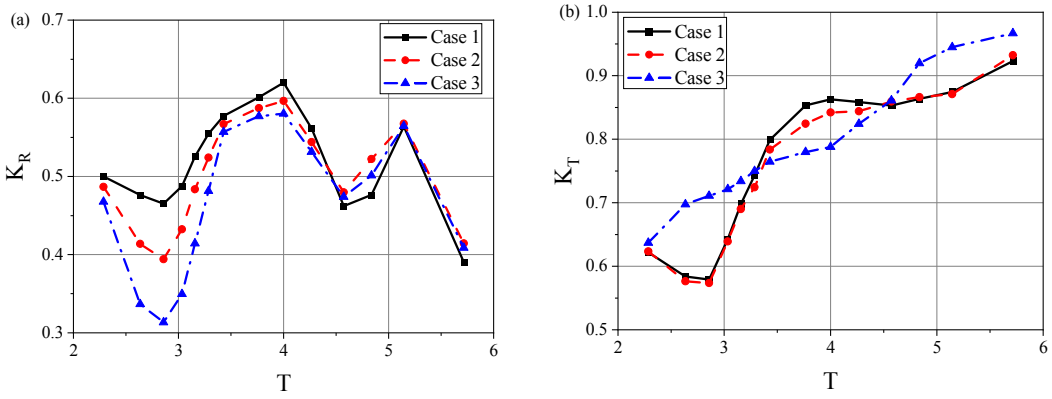

Fig. 21. Variations of (a) wave reflection coefficient K_R and (b) transmission coefficient K_T versus non-dimensional wave period T for different moonpool sizes

4.5 Effect of incident wave direction

To study the effect of the incident wave direction on the hydrodynamic of the multi-purpose platform, numerical simulations are conducted for three different incident wave angles θ with wave height H_I=0.1, while the other parameters remain the same as Case 3 in Section 4.4. Fig. 22 gives the variation of heaving motion amplitude of each WEC with wave period. It can be observed that the motion responses of WEC 1 increase with increasing incident wave angle in the long wave region, while they tend to merge together in the extremely long-wave region. This is because the thickness of the connecting wall between two pontoons is significantly smaller than the width of the front pontoon, and thus oblique short waves transmit into the moonpool more easily to cause internal fluid resonance. In extremely long waves, each axis-symmetric WEC heaves in phase with incident waves and is not sensitive to the direction of wave propagation, which leads to an almost identical motion amplitude. On the other hand, motion responses of WEC 2 decrease with increasing incident wave angle, especially in the short wave region, which is attributed to the energy absorption of WEC 1.

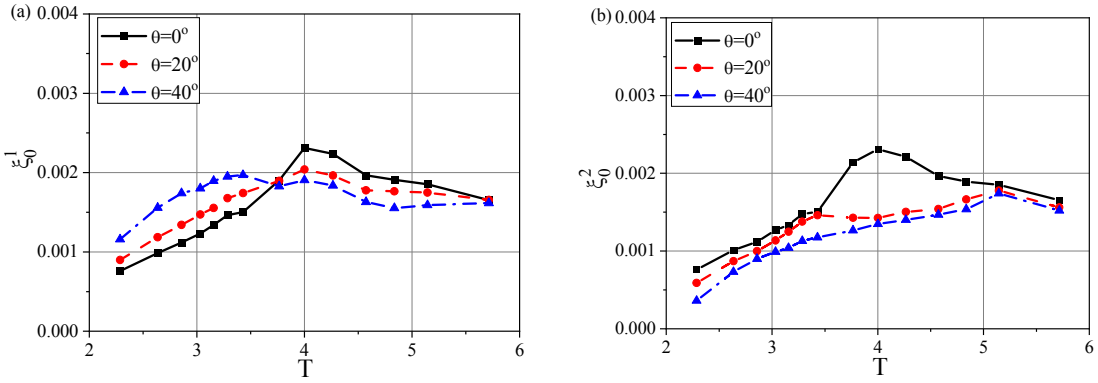

Fig. 22. Variations of motion amplitude ξ_0 versus non-dimensional wave period T for different incident wave angles

Fig. 23 shows the variation of the total average generated power E_p and the capture efficiency R against both wave period and incident wave angle. From these figures, it can be observed that the energy extraction increases with increasing incident wave angle θ in the short wave region, but follows an opposite trend in the longwave region. What's more, the occurring wave periods of the maximum decrease with increasing θ, and are located at T=4 (θ=0°), 3.6 (θ=20°), 3.3 (θ=40°)

corresponding to the capture efficiency of 0.045, 0.039, and 0.041, respectively. This is due to the exchange of the fluid mass from the moonpool to the outer main fluid domain.

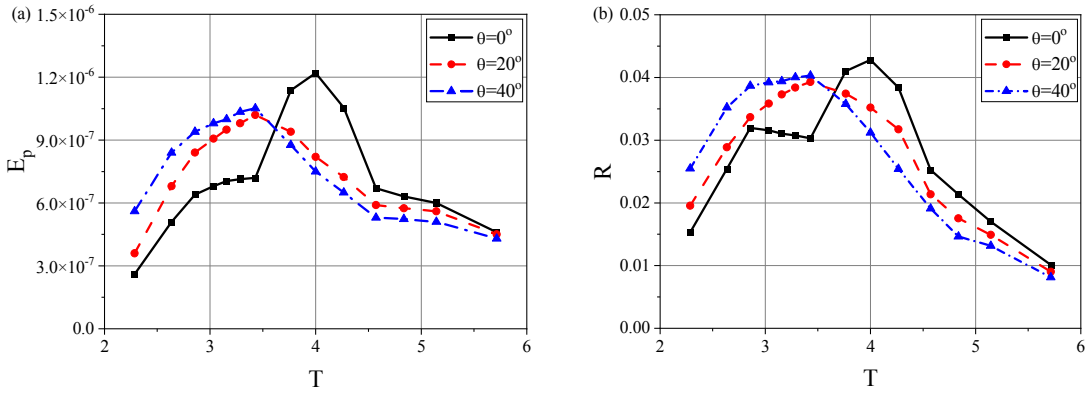

Fig. 23. Variations of (a) the total average generated power E_p and (b) the capture efficiency R versus non-dimensional wave period T for different incident wave angles

Finally, the variation of the reflection coefficient and the transmission coefficient with both wave period and incident wave angle is given in Fig. 24. The results indicate that the reflection coefficient and the transmission coefficient increases and decreases respectively, with increasing incident wave angle over the whole simulated wave period. This is due to the effective wavelength along the direction normal to the body length decreasing with increasing incident wave angle, and further, enhance wave attenuation capacity of the multi-purpose platform.

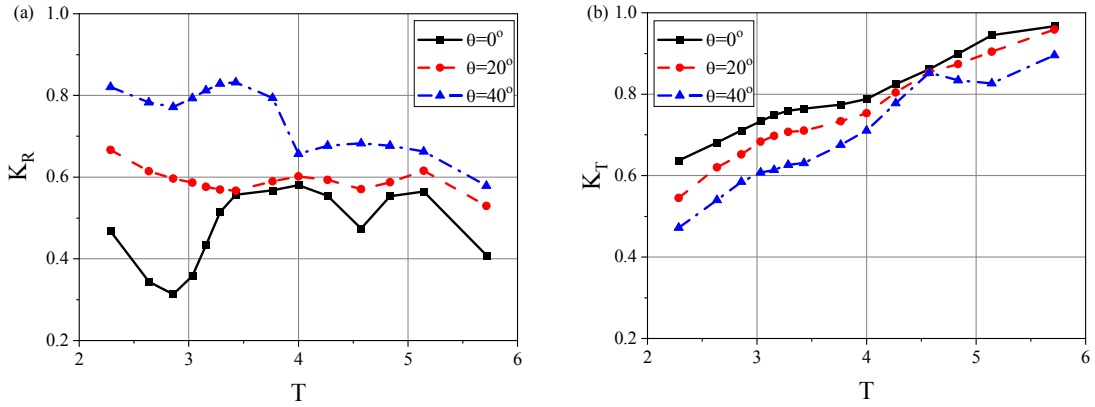

Fig. 24. Variations of (a) wave reflection coefficient K_R and (b) transmission coefficient K_T versus non-dimensional wave period T for different incident wave angles

5. Conclusions

In this study, a novel multi-purpose platform including the advantages and design features of a moonpool-type floating breakwater and an array of heaving OB WECs is proposed, and the corresponding hydrodynamics is investigated using a developed 3D time-domain NWT. The wave attenuation capacity, the wave energy extraction, and the mutual relationship between the breakwater and the WECs are emphatically discussed, respectively. The following conclusions can be obtained from this investigation:

(1) The introduction of the moonpools can increase significantly the heaving response and wave energy extraction of WECs in the long wave region compared to the isolated WEC layouts. This is due to the long waves being transmitted to the moonpools more easily to cause the internal fluid motion. Moreover, due to the wave absorption of the WECs, the wave attenuation capacity of the

multi-purpose floating platform has certain enhancement compared to the single breakwater.

(2) In the multi-purpose floating platform, the WECs with larger diameter can capture more wave energy, while the transmission coefficient is not very sensitive to the horizontal dimension of the WEC in the short wave region. The interaction factors with different WEC diameters implies that the wave energy extraction of the WEC is not only improved by the moonpool between two pontoons but also has a positive effect on the total wave attenuation.

(3) Stronger wave nonlinearity reduces the motion responses, the average generated power, the capture efficiency, and the transmission coefficient of the multi-purpose platform, and leads to a smaller optimal PTO damping corresponding to maximum energy extraction. The increase of PTO damping cannot affect the reflection coefficient but can reduce the transmission at a large wave amplitude.

(4) Thinner moonpools play a more dominant role in wave energy conversion than fatter moonpools for an unequal layout of moonpools, especially in the short wave region because the internal fluid resonance in the moonpool becomes stronger. By adjusting the moonpool length and the moonpool number in a multi-purpose platform, the whole floating system can broaden the effective bandwidth for a practical wave farm.

(5) Oblique waves amplify wave energy extraction of the multi-purpose platform in the short wave region due to a more violent mass exchange of fluid from the moonpool to the outer domain. In addition, the wave attenuation capacity in oblique waves can be improved as a result of reduced effective wavelength in the normal direction of the platform length.

The novel conceptual design of the multi-purpose platform system can provide a promising way to achieve the synergies between offshore infrastructural protection and wave energy utilization, helping to guide geometric configuration design and commercial operation as soon as possible. The developed nonlinear time-domain model can be used as an accurate numerical tool for parametric optimization, durability analysis, and comparison with tested data. Future studies will focus on extending the model to simulate irregular wave conditions which may have seasonal physical characteristics.

CRediT authorship contribution statement

Yong Cheng: Methodology, Software, Data curation, Writing-original draft, Supervision. **Chen Xi:** Validation, Formal analysis, Writing-original draft, Investigation. **Saishuai Dai:** Formal analysis, Data curation, Writing-review & editing, Supervision. **Chunyan Ji:** Writing-review & editing, Supervision, administration. **Margot Cocard:** Formal analysis, Data curation, Writing-review & editing. **Zhiming Yuan:** Writing-review &editing. **Atilla Incecik:** Supervision.

Declaration of Competing Interest

The authors declare that they have no known competing financial interests or personal relationships that could have appeared to influence the work reported in this paper.

Acknowledgment

The authors are grateful to the National Natural Science Foundation of China (Grant No. 52025112, 51861130358, 51609109), the State Key Laboratory of Ocean Engineering, China (Shanghai Jiao Tong University) (Grant No. 1905) and the Newton Advanced Fellowships (Grant No. NAF\R1\180304) by the Royal Society for supporting this work.

References

[1] International Energy Agency (IEA). Renewables 2020 Data Explorer: https://www.iea.org/articles/renewables-2020-data-explorer?mode=market&region=World&product=Total, 2020.

[2] Ferro BD. Wave and tidal energy. Refocus 2006; 7(3): 46-48.

[3] Ning DZ, Wang RQ, Zou QP, Teng B. An experimental investigation of hydrodynamics of a fixed OWC Wave Energy Converter. Appl Energy 2016; 168: 636-648.

[4] Neelamani S, Natarajan R, Prasanna DL. Wave interaction with floating wave energy caisson breakwaters. J Coast Res 2006; 22(2): 745-749.

[5] He F, Huang ZH, Law AW. Hydrodynamic performance of a rectangular floating breakwater with and without pneumatic chambers: An experimental study. Ocean Eng 2012; 51: 16-27.

[6] He F, Huang ZH, Law AW. An experimental study of a floating breakwater with asymmetric pneumatic chambers for wave energy extraction. Appl Energy 2013; 106: 222-231.

[7] Howe D, Nader JR, Macfarlane G. Performance analysis of a floating breakwater integrated with multiple oscillating water column wave energy converters in regular and irregular. Appl Ocean Res 2020; 99: 102147.

[8] Xu CH, Huang ZH. A dual-functional wave-power plant for wave-energy extraction and shore protection: a wave-flume study. Appl Energy 2018; 229: 963-976.

[9] Zheng SM, Zhang YL, Iglesias G. Coast/breakwater-integrated OWC: a theoretical model. Marine Struct 2019; 66: 121-135.

[10] Ning DZ, Zhao XL, Göteman M, Kang HG. Hydrodynamic performance of a pile-restrained WEC-type floating breakwater: An experimental study. Renew Energy 2016; 95: 531-541.

[11] Zhao XL, Ning DZ, Zhang C, Kang HG. Hydrodynamic investigation of an oscillating buoy wave energy converter integrated into a pile-restrained floating breakwater. Energies 2017; 10(5): 712.

[12] Madhi F, Yeung RW. On survivability of asymmetric wave-energy converters in extreme waves. Renew Energy 2018; 119: 891-909.

[13] Ning DZ, Zhao XL, Zhao M, Hann M, Kang HG. Analytical investigation of hydrodynamic performance of a dual pontoon WEC-type breakwater. Appl Ocean Res 2017; 65: 102-111.

[14] Martinelli L, Ruol P, Favaretto C. Hybrid structure combining a wave energy converter and a floating breakwater. In: Proceedings of the International Offshore and Polar Engineering Conference 2016: 622-628.

[15] Nguyen HP, Wang CM, Pedroso DM. Optimization of modular raft WEC-type attachment to VLFS and module connections for maximum reduction in hydroelastic response and wave energy production. Ocean Eng 2019; 172: 407-421.

[16] Zhang HC, Xu DL, Zhao H, Xia SY, Wu YS. Energy extraction of wave energy converters embedded in a very large modularized floating platform. Energy 2018; 158: 317-329.

[17] Reabroy R, Zheng XB, Zhang L, Zang J, Yuan Z, Liu MY, Sun K, Tiaple Y. Hydrodynamic response and power efficiency analysis of heaving wave energy converter integrated with breakwater. Energ Convers Manage 2019; 195: 1174-1186.

[18] Zhang CW, Ning DZ. Hydrodynamic study of a novel breakwater with parabolic openings for wave energy harvest. Ocean Eng 2019; 182: 540-551.

[19] Ning DZ, Shi J, Zou QP, Teng B, Investigation of hydrodynamic performance of an OWC (oscillating water column) wave energy device using a fully nonlinear HOBEM (higher-order boundary element method). Energy 2015; 83: 177-188.

[20] Shi ZY, Xiao HS, Zhu QF, Wang QS. Resonant frequencies analysis and vibration control of fluid in three-dimensional (3D) moonpool: Analytical modeling and experimental study. Mech Syst Signal Pr 2020; 144: 106882.

[21] Ravinthrakumar S, Kristiansen T, Molin B, Ommani B. Coupled vessel and moonpool responses in regular

and irregular waves. Appl Ocean Res 2020, 96: 102010.

[22] Bull D. An improved understanding of the natural resonances of moonpools contained within floating rigid-bodies: Theory and application to oscillating water column devices.

[23] Zheng SM, Zhang YL, Iglesias G. Concept and performance of a novel wave energy converter: Variable Aperture Point-Absorber (VAPA). Renew Energy 2020; 153: 681-700.

[24] Liu ZQ, Wang YZ. Numerical investigations and optimizations of typical submerged box-type floating breakwaters using SPH. Ocean Eng 2020; 209: 107475.

[25] Li HB, Han GM, Mang HA. A new method for evaluating singular integrals in stress analysis of solids by the direct boundary element method. Int J Numer Methods Eng 1985; 211: 2071-2075.

[26] Cheng Y, Ji CY, Zhai GJ. Fully nonlinear analysis incorporating viscous effects for hydrodynamics of an oscillating wave surge converter with nonlinear power take-off system, Energy 2019;179:1067-1081.

[27] Cheng Y, Li G, Ji CY, Fan TH, Zhai GJ. Fully nonlinear investigations on performance of an OWSC (oscillating wave surge converter) in 3D (three-dimensional) open water. Energy 2020; 210: 118526.

[28] Goda Y, Suzuki Y. Estimation of incident and reflected waves in random wave experiments. In: Proceedings of the 15th International Conference on Coastal Engineering ASCE 1976: 828-845.

[29] Wu, Y.S., Ding J., Gu X.K., Tian C, Ye YL, Cheng XM, et al. The progress in the verification of key technologies for floating structures near islands and reefs. Proceedings of the Thirtieth International Ocean and Polar Engineering Conference, Shanghai, China, 2020.

[30] Hu JJ, Zhou BZ, Vogel C, Liu P, Willden R, Sun K, et al. Optimal design and performance analysis of a hybrid system combing a floating wind platform and wave energy converters. Appl Energy 2020; 269: 114998.

[31] Zhao XL, Ning DZ. Experimental investigation of breakwater-type WEC composed of both stationary and floating pontoons. Energy 2018; 155:226-233.

[32] Ning DZ, Zhao XL, Zhao M, Hann M, Kang HG. Analytical investigation of hydrodynamic performance of a dual pontoon WEC-type breakwater. Appl Ocean Res 2017; 65:102-111.